CHARACTERIZING EARLY TIME FRACTURE INTERFERENCE EFFECTS AND LATE TIME RESERVOIR SHAPE FACTOR EFFECTS USING ANALYTICAL METHODS

An Undergraduate Research Scholars Thesis

by

NUTCHAPOL DENDUMRONGSUP and NIAN WEI TAN

Submitted to the Undergraduate Research Scholars program at
Texas A&M University
in partial fulfillment of the requirements for the designation as an

UNDERGRADUATE RESEARCH SCHOLAR

Approved by Research Advisor: Dr. Michael King

May 2017

Major: Petroleum Engineering

TABLE OF CONTENTS

ABSTRACT

Characterizing Early Time Fracture Interference Effects and Late Time Reservoir Shape Effects Using Analytical Methods

Nutchapol Dendumrongsup and Nian Wei Tan
Department of Petroleum Engineering
Texas A&M University

Research Advisor: Dr. Michael King
Department of Petroleum Engineering
Texas A&M University

Based on the asymptotic approximation of the diffusivity equation for slightly compressible fluids, our research team looked into its application in early time fracture interference effects and late time reservoir shape factor effects.

Hydraulic fracturing is a common completion technique for modern horizontal wells. The effect of fracture interference comes into play when producing fractures influence each other's performance due to close proximity. The issue is of great interest to the industry as fracture interference negatively affects production and cost, making optimal fracture spacing a very attractive research topic. In this work, we intend to characterize fracture interference effects using analytical methods. We found that by using the concepts of rate-normalized pressure and material balance time, we are able to calculate the individual drainage volume of each fracture. We proposed a methodology to summarize individual fracture drainage volume to represent the total well drainage volume.

Moreover, the behavior of the pressure will also be investigated during the late time when the boundaries influence the pressure drop. Currently, the method to identify the average reservoir pressure is called Diez shape factor. However, Dietz shape factor did not offer an

understanding of the interaction between the pressure wave and boundary. It is also limited by the fact that raw bottom hole pressure cannot be directly used to measure the average reservoir pressure. The conventional shape factor is also limited by simple geometry shape. In our research, we attempted to use the asymptotic equation of diffusivity equation to determine the new shape factor. The involved process will help us learn about pressure wave interaction and the resulted shape factors will be applicable for any reservoir shape.

ACKNOWLEDGEMENTS

We would like to thank our advisor, Dr Michael King for his invaluable guidance throughout the course of this research. We also would like to acknowledge the help of several graduate student in the MCERI research group that also help on our research. We also want to thank our friends and colleagues for their support and confidence throughout our study at Texas A&M University.

NOMENCLATURE

x_f	Fracture half length, distance from centre of fracture to fracture tip, ft
q_w	Flow rate observed at the wellbore, stb/day
Δp	Pressure drop, psi
ΔRNP	Rate-normalized pressure drop $\left(\frac{\Delta p}{q_w}\right)$, psi*day/stb
V_d	Drainage volume, bbl
c_t	Total compressibility, sum of rock and fluid compressibility, 1/psi
N_p	Cumulative production, i.e. sum of produced fluids, stb
t_e	Material balance time $\left(\frac{\mathrm{N_p}}{q_w}\right)$, days or hrs

CHAPTER I

INTRODUCTION

On Fracture Interference

Modern horizontal wells are often produced with hydraulic fracturing, i.e. creating fractures perpendicular along the wellbore to maximize reservoir contact area. Each fracture will produce independently until the pressure response produced by each fracture begins to affect each other.

Characterizing reservoir performance during fracture interference was not a pressing concern in the last few decades when the world produced mostly from conventional reservoirs. In conventional reservoirs, the drainage volume seen from the well expands beyond the fracture geometry rapidly. After a short time span of a few hours to a few days, the drainage volume expands beyond the geometry of the individual fractures and evolves into a single composite drainage volume independent of fracture characteristics. In other words, the performance of the well no longer depends on the fractures, but on the quality of the reservoir. However, in unconventional reservoirs, pressure fronts propagates slowly. The effects of the fracture geometry can be still dominating the well performance in the time span of a few years to a few decades.

With the advent of hydraulic fracturing and horizontal well technology, unconventional reservoirs are starting to grow as a dominant source of oil and gas. Currently, there is little understanding about unconventional reservoir dynamics, especially in terms of fracture interference. Unconventional reservoir flow constitute nonlinear behavior of multiphase flow in extremely low permeability rock, coupled with other processes that do not exist in conventional

wells such as non-Darcy flow and rock-fluid interaction within tiny pores or micro-fractures. Hence, in addition to the motivations listed above, there is an academic interest in quantifying the effect of fracture interference.

On Reservoir Shape Effects

After the infinite acting radial flow, it is important to be able to determine the average reservoir pressure so that the size of the reservoir may be determined from material balance calculations and the approximate distribution of pressure within a reservoir for detection of fluid movement can be define. The average pressure in the drainage volume can be attained by extrapolating to infinite time the linear portion of the graph of closed-in pressure versus the logarithmic function of the Horner time ratio. Dietz presented a method for determining average reservoir pressure, which is simpler to apply than that devised by previous method. However, it depends upon the assumption that previous production history is immaterial once a steady state has been attained based on the shape of the graph obtained by the previous work. After our model has been calibrated, to the conventional method to determine the shape factor, our group will attempt to determine the shape factor for more various shapes and settings of the reservoirs and wells locations.

CHAPTER II

CHARACTERIZING EARLY TIME FRACTURE INTERFERENCE EFFECTS

Classic Drainage Volume

We intend to derive our methodology based on drainage volume, since it reflects the physical phenomenon of pressure propagation in the reservoir. Drainage volume is classically defined by Matthews, Brons and Hazebroek (1965) as the volume of a reservoir drained by a well when the reservoir is in boundary-dominated flow. During boundary-dominated flow, each well in the reservoir drains from an acreage that is proportional to its flow rate, as illustrated in **Fig 2.1**.

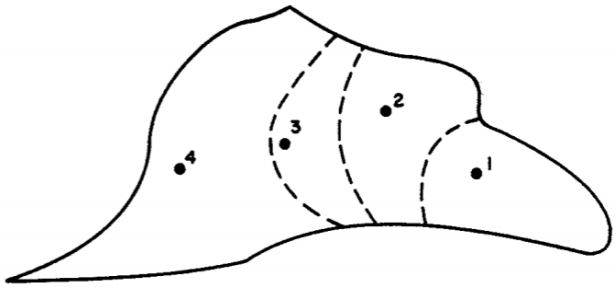

Fig 2.1 – Each well draining a part of the reservoir proportional to its flow rate during boundary-dominated flow

Transient Drainage Volume

The MCERI (Model Calibration and Efficient Reservoir Imaging) research group at Texas A&M University has extended the concept of drainage volume to transient flow by introducing a transient term that varies with time and distance from flux source. Following Yang et al (2015), the asymptotic approximation to the diffusivity equation for slightly compressible fluids gives us **Eqn 2.1**:

$$c_t \frac{\partial \Delta p}{\partial t} = \frac{q_w}{V_d(t)} e^{-\frac{r^2}{4\alpha t}} \ldots\ldots (2.1)$$

By taking the measurement at the wellbore, we substitute an extremely small number for r, reducing the exponential term to unity, as shown in **Eqn 2.2**.

$$c_t \frac{\partial \Delta p}{\partial t} = \frac{q_w}{V_d(t)} \ldots\ldots (2.2)$$

With some algebra, we obtain an expression for drainage volume in terms of flow rate and pressure drop derivative in **Eqn 2.3**.

$$V_d(t) = \frac{q_w}{c_t} * \frac{d\Delta p}{dt}^{-1} \ldots\ldots (2.3)$$

Reservoir Model Construction

With this methodology in mind, we constructed a synthetic reservoir with three fractures of similar length and orientation. The wellbore and fractures are assumed to have infinite conductivity, i.e. have no pressure drop between themselves. Hence, by definition all three fractures will have the same bottomhole pressure. We observed interference effects causing the flow to be unevenly distributed between the fractures, as shown in **Fig 2.2**.

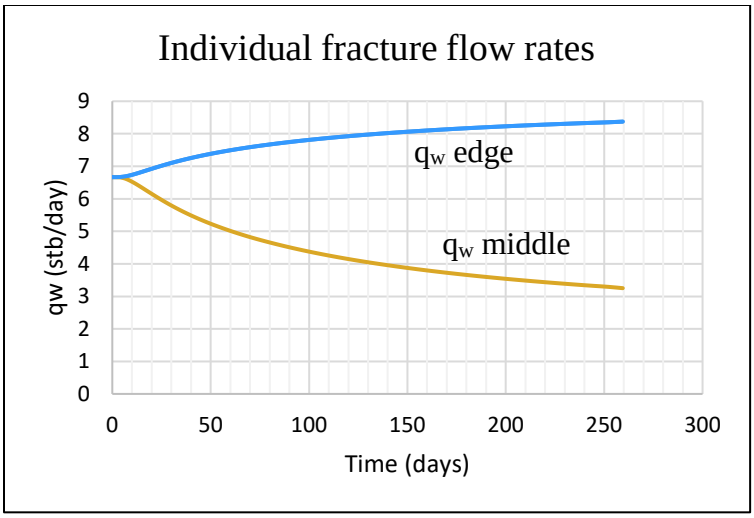

Fig 2.2 – Comparison of individual fracture flow rates

Rate-Normalized Pressure Concept

We wish to extend the concept of transient drainage volume to be used on fractures. As shown in Fig 2.2 above, individual fracture flow rates are variable with time, while the expression of drainage volume derived in Eqn 2.3 requires constant flow rate input. Using the concepts of Rate-Normalized Pressure derived by Winestock and Colpitts (1965), we adapt Eqn 2.1 for variable flow rates. It is an approximation that works reasonably well for smoothly variable rates, which applies to the case of fracture interference. Substituting Rate-Normalized Pressure for pressure drop gives us **Eqn 2.4**:

$$\boldsymbol{V_d(t) = \frac{1}{c_t} * \left(\frac{d}{dt} \frac{\Delta p}{q_w} \right)^{-1}} \quad \ldots\ldots (\mathbf{2.4})$$

In addition, Rate-Normalized Pressure plays an additional role in incorporating interference effects. Since our infinite conductivity fractures and wellbore are defined to have the same pressure drop everywhere, using Rate-Normalized Pressure allows us to differentiate

between individual fracture production, and scale fracture drainage volumes with respect to their flow rates.

Material Balance Time Concept

We propose to combine individual fracture performance by applying the concept of superposition, introduced in Lee et al. (2003) to combine variable production into a quantitatively representative production schedule. However, calculating superposition time requires specific knowledge of the flow regime in the reservoir. To avoid making assumptions about the flow regime, we use material balance time as adopted by Palacio and Blasingame (1993) to approximate superposition time. Material Balance Time denotes the amount of time that needs to pass, assuming that all of the fluids produced are done at the instantaneous flow rate.Material balance time is given in **Eqn 2.5** below:

$$\boldsymbol{t_e = \frac{N_p}{q_w}} \ldots\ldots (\mathbf{2.5})$$

Aside from providing a tool to summarize fracture performance, Material Balance Time incorporates interference effects by scaling the timeline of each fracture with respect to individual fracture flow rates. Fractures that are producing more will be effectively "slowed down" due to the larger denominator term, and vice versa. Substituting material balance time for observed time gives us **Eqn 2.6**:

$$\boldsymbol{V_d(t) = \frac{1}{c_t} * \left(\frac{d}{dt_e}\frac{\Delta p}{q_w}\right)^{-1}} \ldots\ldots (\mathbf{2.6})$$

Calculating Individual Fracture Drainage Volume

Applying Eqn 2.6 to each fracture allows us to calculate individual fracture drainage volume. The results are shown below in **Fig 2.3**.

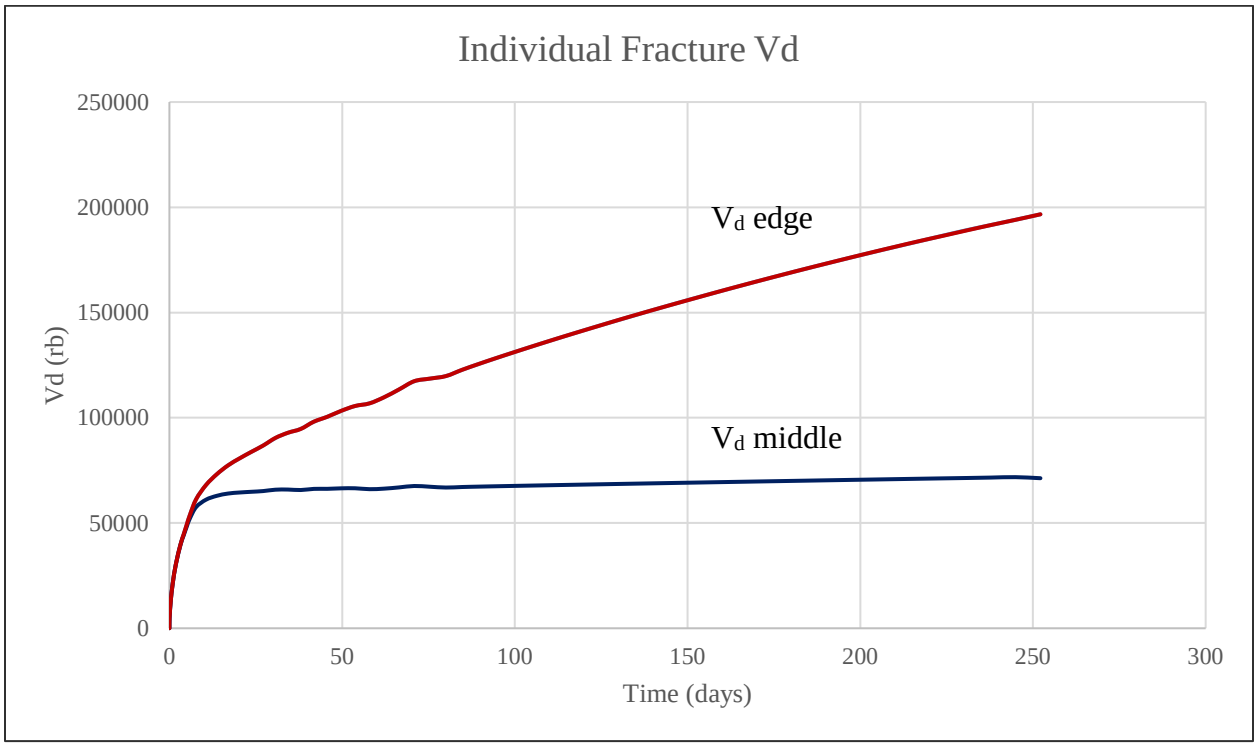

Fig 2.3 – Comparison of individual fracture drainage volumes for 3 fracture case

From Fig 2.3, we can see that the initial individual drainage volumes are similar until the onset of interference. On one hand, the drainage volume of the fracture in the middle approaches an asymptote after interference begins. We postulate that it is bound by the drainage volumes of the fractures on the edges, and thus is unable to access more of the reservoir. After interference begins, these middle fractures stop contributing significantly to drainage volume growth. On the other hand, the drainage volume of the fractures on the edge are allowed to continue to grow and access more of the reservoir, albeit at a slower rate than before due to interference.

Extending the methodology to a reservoir model with 21 fractures shown in **Fig 2.4** show that our observations are consistent across the number of fractures, and can be applied in real-world scenarios where we are looking at two-digit fracture counts. Fig 2.4 also validates our approach in categorizing fractures as middle fractures and edge fractures, as it is shown that the behavior of a fracture is only dependent on their relative position to other fractures.

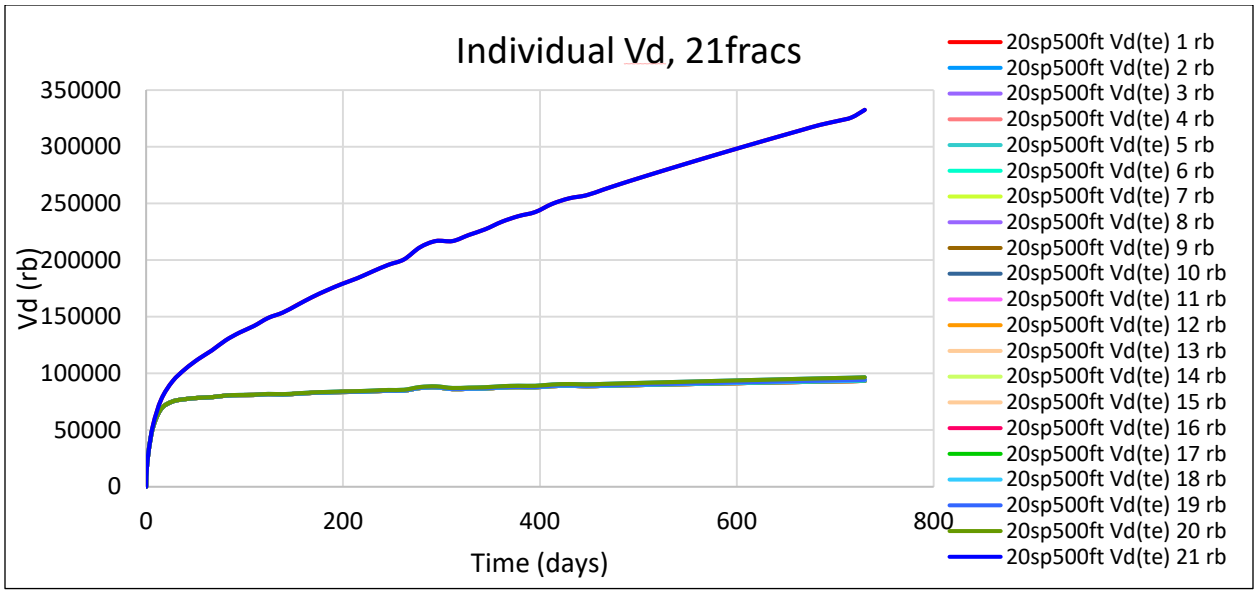

Fig 2.4 – Comparison of individual fracture drainage volumes for 21 fracture case

Interpreting Individual Fracture Drainage Volume

We plot the pressure derivatives for the edge fractures and middle fracture on a diagnostic plot (**Fig 2.5**) to observe the flow regimes. Initially, we observe a slope of ½ in the pressure derivative for both fracture types. This indicates that the fractures are producing from linear flow, which is a signature of early-time fracture production.

After the onset of interference, we observe a constriction in drainage volume for both fracture types, as shown by the increase in the pressure derivatives. On one hand, the slope of the pressure derivative for the edge fractures changes from ½ to around ¾. The slope does not

change completely to match any known flow regime signatures, which indicates transition to a mixed flow regime. We infer that this is due to the edge fractures being bounded on the side facing the middle fracture, and unbounded on the opposite side. The bounded side would see fracture interference, while the unbounded side would continue to expand into the reservoir.

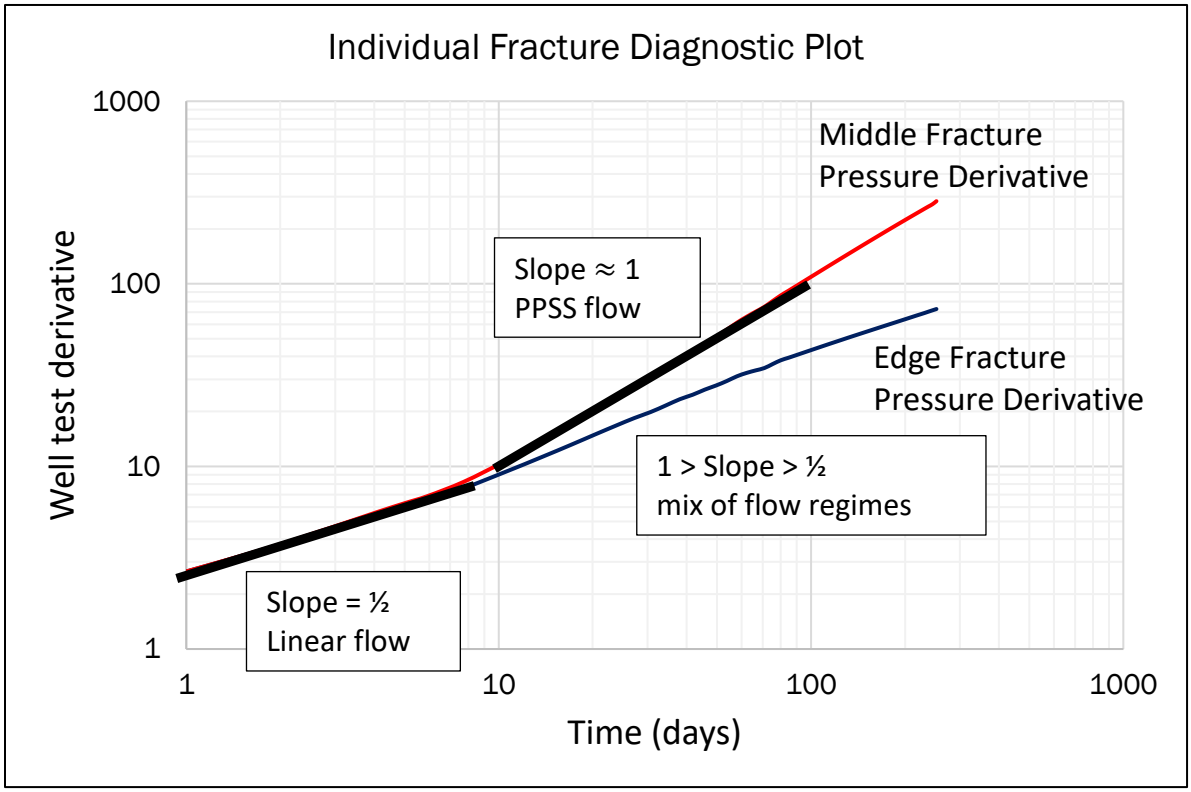

Fig 2.5 – Comparing the flow regimes of edge fractures and middle fracture

On the other hand, the pressure derivative of the middle fracture is shown to approach a slope of 1 at onset of interference. Upon closer inspection, we discovered that the slope only approximates 1 but is not exact. This is a characteristic of pseudo pseudo-steady state flow (PPSS), as defined by Song and Economides (2011), wherein the collision of two fracture linear flow regimes cause an upwards deflection with a slope near 1.

Comparing Flow Regime Observations with SPE-140555

We compared our fracture flow regime observations with the flow regime observations in SPE-140555, shown in **Fig 2.6**.

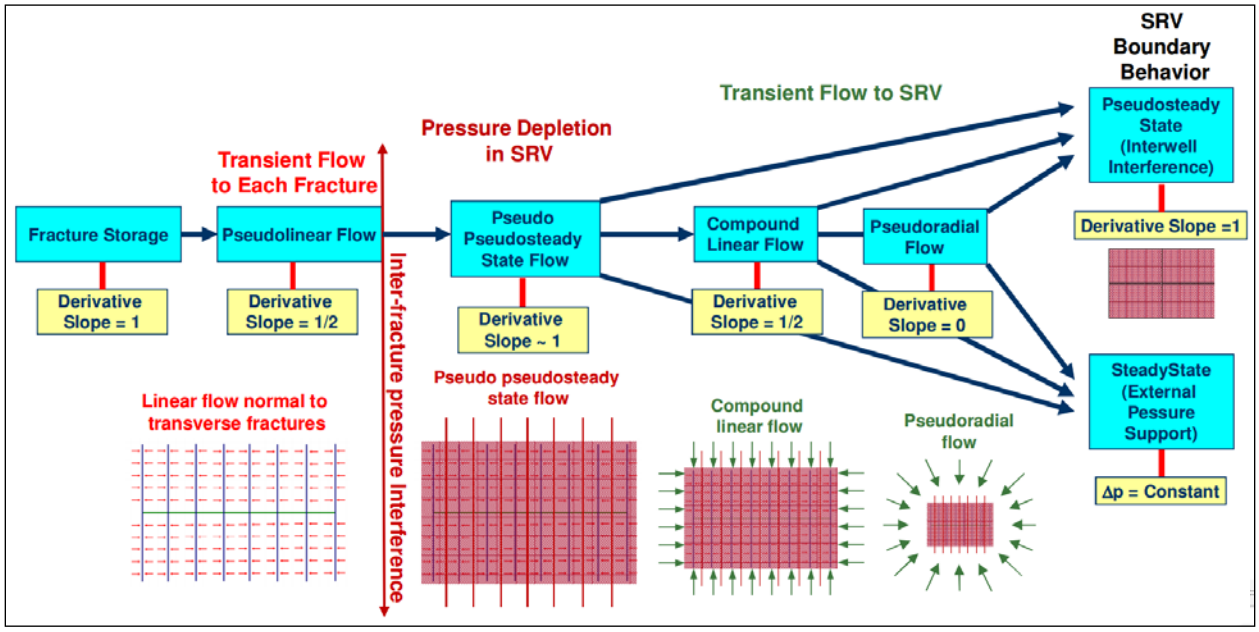

Fig 2.6 – Typical fracture flow regimes, SPE-140555

Our observations generally agree with SPE-140555 except for the reservoir pseudo pseudosteady state flow and compound linear flow.

SPE-140555 observes that the reservoir as a whole enters pseudo pseudosteady state flow after interference begins. The reservoir then progresses to compound linear flow, where it will observe flow from all sides, as shown in **Fig 2.7**.

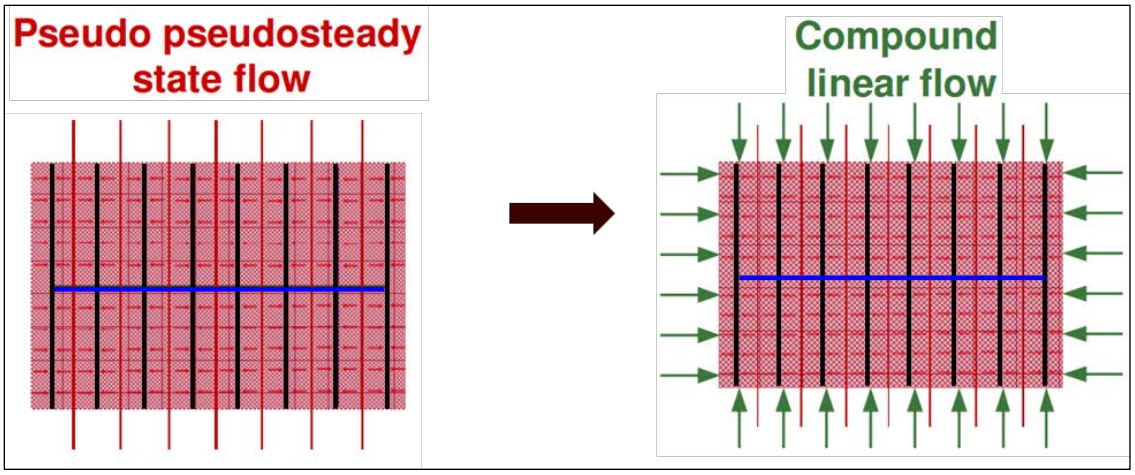

Fig 2.7 – Progression of reservoir flow regime after onset of interference

From our observations, we noted that after the onset of interference, only the middle fractures enter pseudo pseudosteady state flow while the edge fractures enter a mixed flow regime, as shown in Fig 2.5. This runs contrary to the observation in SPE-140555 that shows the whole reservoir progressing to pseudo pseudosteady state flow. In addition, we noted that the middle fractures asymptote and stop contributing to drainage volume growth after interference begins, as shown in Fig 2.3. This disagrees with the observation in SPE-140555 that shows middle fractures making flow contributions in compound linear flow.

We propose replacing the pseudo pseudosteady state flow regime and compound linear flow regime with a single linear flow regime, shown in **Fig 2.8**. Upon onset of interference, middle fractures will see pseudo pseudosteady state flow and have negligible contribution to reservoir flow. The edge fractures will continue to grow in drainage volume and contribute to reservoir flow, effectively creating linear flow along the well lateral.

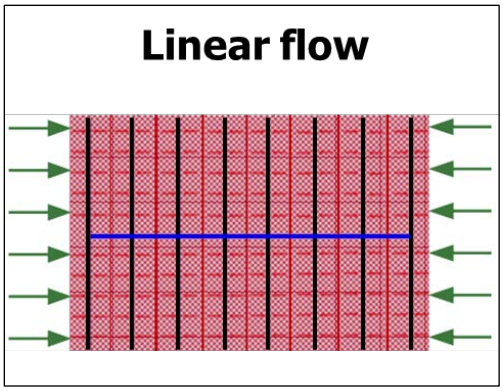

Fig 2.8 – Proposed flow regime to replace Fig 2.7

Calculating Well Drainage Volume

To summarize individual fracture drainage volumes into well drainage volume, we propose performing superposition, i.e. summing up the individual fracture drainage volumes calculated in the previous sections. We benchmarked our proposed method against a theoretical upper bound and lower bound. The equations used are shown below as **Eqn 2.7**, **Eqn 2.8**, and **Eqn 2.9**.

$$\boldsymbol{Upper\ bound}: \boldsymbol{V_d(t)} = \sum_{\boldsymbol{i=1}}^{\boldsymbol{n}} \frac{\boldsymbol{1}}{\boldsymbol{c_t}} * \left(\frac{\boldsymbol{d}}{\boldsymbol{dt}} \frac{\boldsymbol{\Delta p}}{\boldsymbol{q_i}}\right)^{\boldsymbol{-1}} \ldots\ldots (\boldsymbol{2.7})$$

$$\boldsymbol{Proposed}: \boldsymbol{V_d(t)} = \sum_{\boldsymbol{i=1}}^{\boldsymbol{n}} \frac{\boldsymbol{1}}{\boldsymbol{c_t}} * \left(\frac{\boldsymbol{d}}{\boldsymbol{dt_e}}\Big|_{\boldsymbol{i}} \frac{\boldsymbol{\Delta p}}{\boldsymbol{q_i}}\right)^{\boldsymbol{-1}} \ldots\ldots (\boldsymbol{2.8})$$

$$\boldsymbol{Lower\ bound}: \boldsymbol{V_d(t)} = \frac{\boldsymbol{1}}{\boldsymbol{c_t}} * \left(\frac{\boldsymbol{d}}{\boldsymbol{dt}} \frac{\boldsymbol{\Delta p}}{\boldsymbol{q_w}}\right)^{\boldsymbol{-1}} \ldots\ldots (\boldsymbol{2.9})$$

For the upper bound, we chose to take the sum of the unadjusted individual fracture drainage volumes. Once interference begins, this quantity will be larger than the actual drainage volume because it sums volumes that potentially overlap. For the lower bound, we calculate the

well drainage volume by ignoring fracture geometry and using well flow rates directly. Wells with fractures should always see a larger drainage volume than wells without fractures. The physical significance of all three methods are illustrated in **Fig 2.9** below.

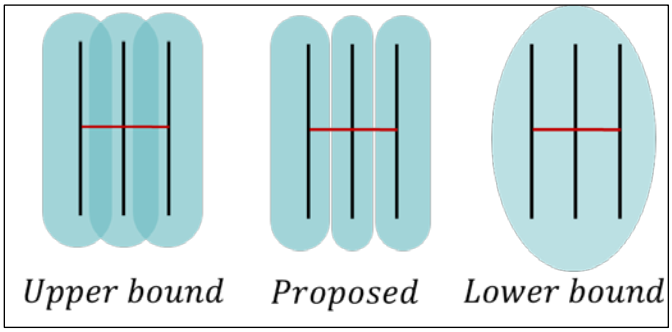

Fig 2.9 – Physical significance of all three methods to calculate well drainage volume.

Plotting the well drainage volumes calculated using all three methods gives us **Fig 2.10** below:

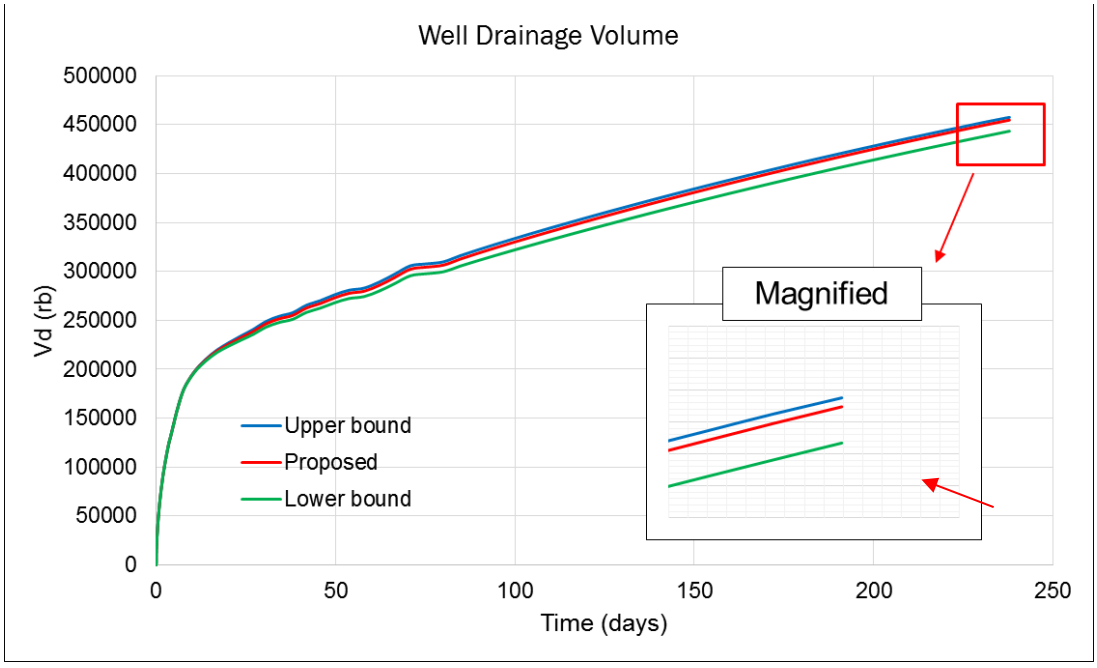

Fig 2.10 – Well Drainage Volume calculated using proposed methodology, upper bound and lower bound

The quantities plotted in the figure above, in order from top to bottom, are the upper bound, proposed methodology and lower bound. It is shown that our proposed methodology sits between our established theoretical upper bound and lower bound.

Extending our well drainage volume calculations to 11 fracture, 21 fracture and 31 fracture cases (**Fig 2.11**, **Fig 2.12**, **Fig 2.13**), we observe that our proposed methodology also fits between our upper and lower bounds. This shows that our proposed methodology is consistent across increasing number of fractures, and is thus reasonable.

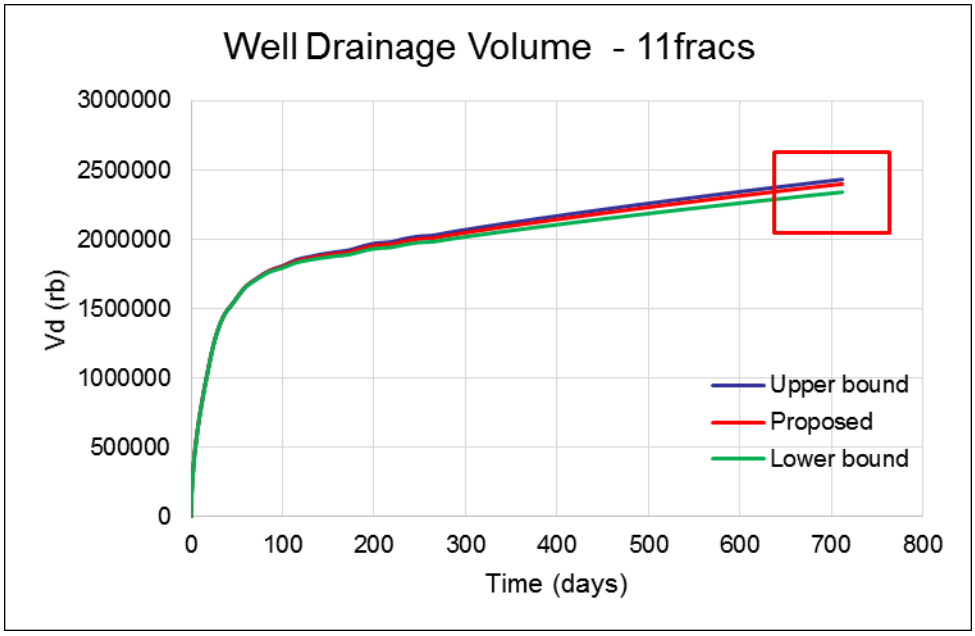

Fig 2.11 – Well drainage volume calculated for 11 fracture case

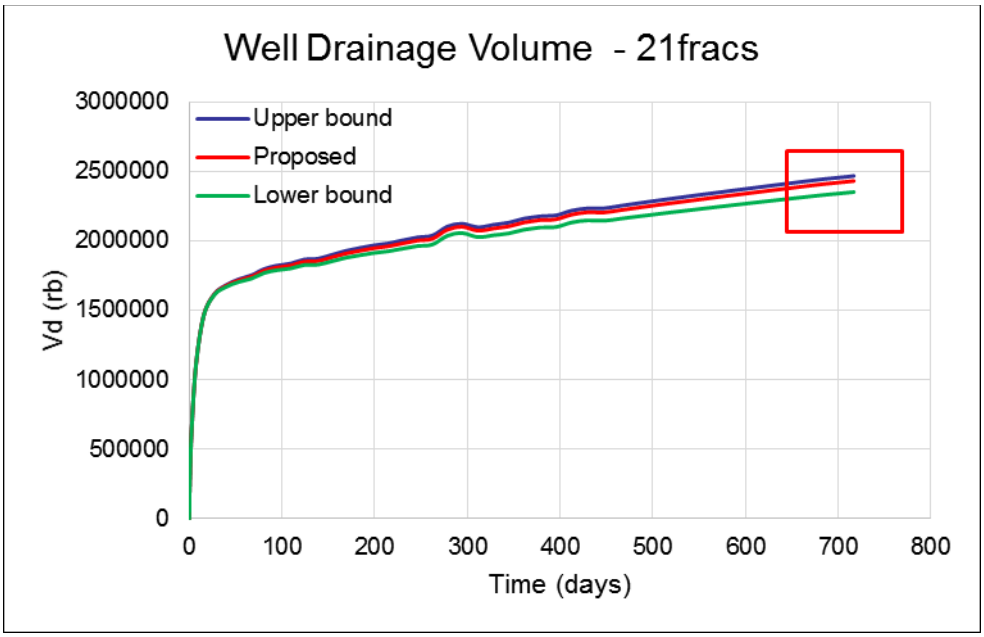

Fig 2.12 – Well drainage volume calculated for 21 fracture case

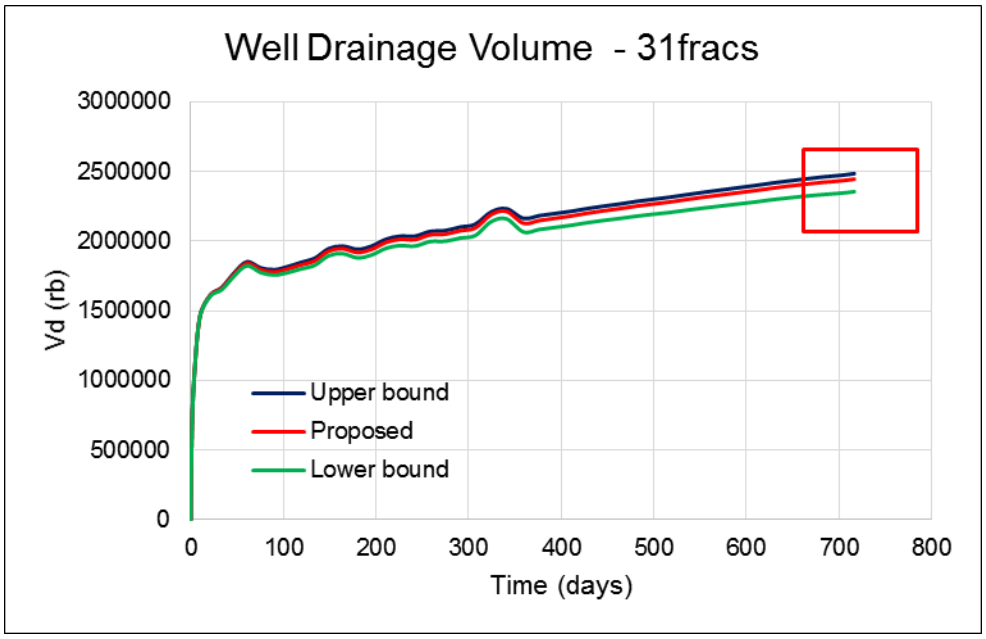

Fig 2.13 – Well drainage volume calculated for 31 fracture case

CHAPTER III

RECALCULATING CLASSIC RESERVOIR SHAPE FACTOR

C.S Matthews, F. Brons, and P. Hazebroek (1954) presented the methodology to obtain the average pressure in the bounded reservoir.

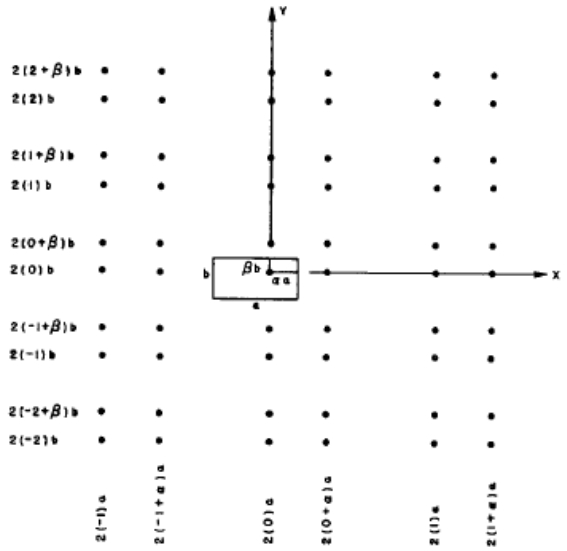

Fig 3.1 The imaginary wells used to calculate the

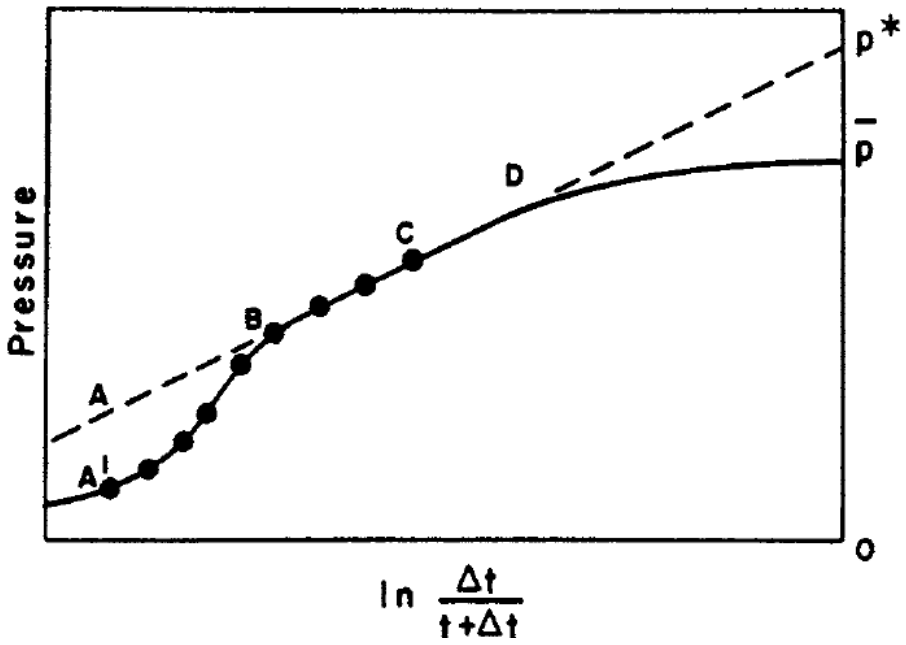

Fig 3.2 Pressure Buildup Curve

The average pressure of the reservoir can be calculated by using the method of the image wells. **Fig 3.1**, for example, shows part of the infinite image net required to simulate the conditions of zero flow across the outer boundary in a rectangle. We can obtain the average pressure of other geometry in the likewise manner. To employ the image well method, the boundary in all four sides will be replaced by the infinite number of image wells. The total pressure drop of the well is the pressure drop of itself if the system is infinite acting radial flow plus all other image wells. The first term of the **Eqn 3.2** is related to the pressure drop of itself and the second term is related to the pressure drop of the infinite image well. Notice that p* is defined as the extrapolation of pressure on the Horner plot as shown in **Fig 3.2**. The long calculation is required to obtain the final form that can be used in the Mathematica to calculate the function that can be used to calculate the pressure drop. The result obtained from Mathematica is used for calibration because the notion of the drainage volume and diffusivity

will be employed to calculate the shape factor that will be applicable in broader limit than the Dietz shape factor that will be presented later in this chapter.

$$\mathbf{p = p_a + \frac{q\mu}{4\pi kh}\left(Ei\left(-\frac{\emptyset\mu c r_w^2}{4k\Delta t}\right) + \sum_{i=1}^{\infty} Ei\left[-\frac{\emptyset\mu c r_w^2}{4k\Delta t}\right]\right) \ldots\ldots (3.1)}$$

$$\mathbf{F(T) = \frac{p^* - p}{\left({}^{q\mu}/_{4\pi kh}\right)} = 4\pi T + \sum_{m,n=-\infty}^{\infty} Ei\left[\frac{a_{m,n}^2}{-4AT}\right] \ldots\ldots (3.2)}$$

$$\mathbf{T = \frac{kt}{\emptyset\mu cA} \ldots\ldots (3.3)}$$

Where $a_{m,n}$ is the distance of the i[th] image well from the well in the reservoir.

$$\boldsymbol{F(T) = 4\pi T - 4\pi T_0 + F(T_0) + \ln\left(\frac{T}{T_0}\right) + image\ term}$$

$$\boldsymbol{image\ term = \left(\frac{1}{\pi}\right) * \left[\int_{T*\pi^2}^{To*\pi^2} \left(\left(2 + 2\sum_{m=1}^{\infty}\left(e^{-m^2\lambda u}(1 + \cos(2m\alpha\pi))\right)\right) * \left(2 + 2\sum_{n=1}^{\infty}\left(e^{-n^2u/\lambda}(1 + \cos(2n\alpha\pi))\right)\right)\right) du\right] (3.4)}$$

Dietz presented a method to determine average reservoir pressure that is simpler to apply than that devised by Matthews, Brons, and Hazebroek. “For bounded reservoirs, identical results are obtained if stabilized-flow conditions prevail. The present method yields inferior results in the transient state.” The method to determine the shape factor for the circular reservoir is presented, which will lead to the notion of the shape factor in other shapes of reservoirs.

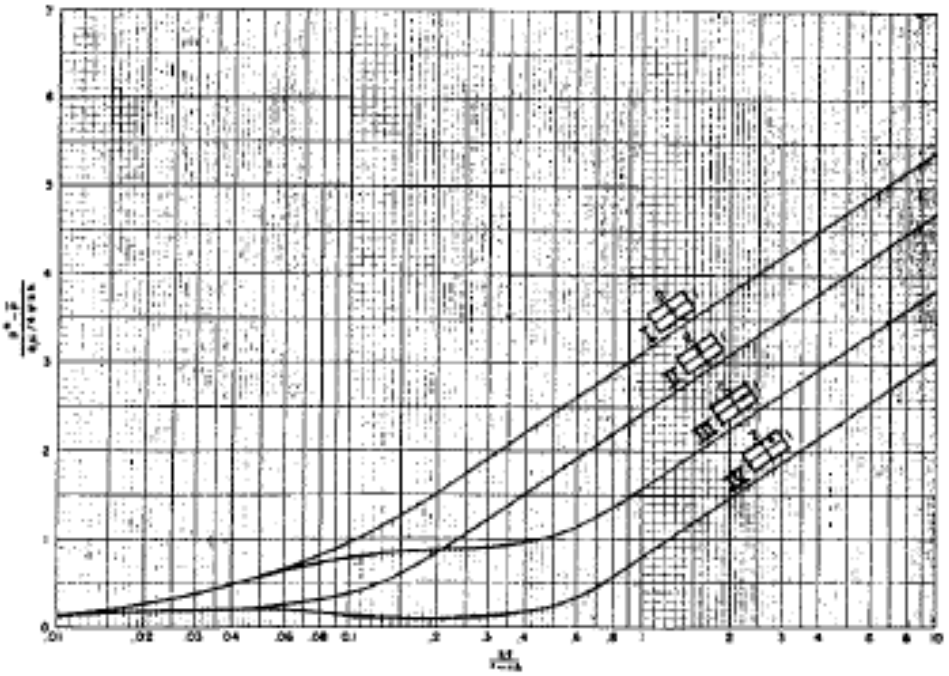

Fig 3.3 Pressure function for different well locations in a 2: 1 rectangular boundary from the MBH paper

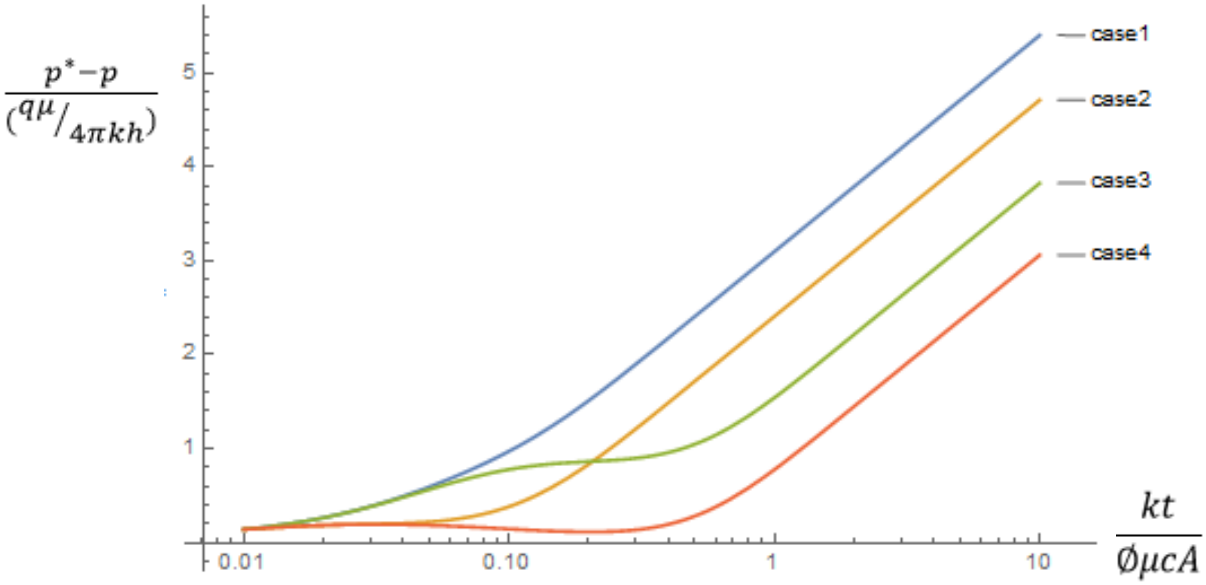

Fig 3.4 Pressure function for different well locations in a 2: 1 rectangular boundary from Mathematica

Dietz notices that the tail of the graphs in **Fig 3.3** is resembled to the straight lines with the unit slope but different x-axis interception. **Fig 3.5** illustrates each investigated setting on **Fig 3.2**.

Therefore, he approximated them as straight line with the following expression

$$\frac{p^* - p}{\left({}^{q\mu}/_{4\pi kh}\right)} = \ln\left(\frac{C_A kt}{\emptyset \mu c A}\right) \dots\dots (3.11)$$

The shape factor C_A can be obtained from the Eq11 when $\frac{kt}{\emptyset \mu c A} = 1$. Therefore,

$$\frac{p^* - p}{\left({}^{q\mu}/_{4\pi kh}\right)} = \ln(C_A) \dots\dots (3.12)$$

Likewise, C_A can be read from the straight-line parts of the curves in **Fig 3.4** at the abscissa value of 1. Mathematica is employed to calibrate the calculate result with the CA results offers by the Dietz paper on **Fig 3.6**. **Table 3.1** shows that the calculated results satisfy with the one provided by the paper. Thus, the code is correct and ready for any further usage. In the next process of the research, T will be replaced by the diffusivity time of fight, which will lead to more robust shape factor that can be applicable in on broader scale.

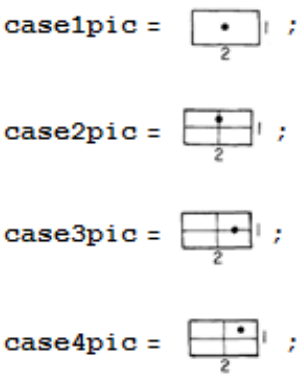

Fig 3.5 Each investigated setting

Table 3.1 Results from the Mathematica compared with ones offered from the paper

case	ln(CA) from calculation	ln (CA) from the paper	difference	% difference
1.0000	3.0979	3.1200	0.0221	0.7080
2.0000	2.4084	2.3800	0.0284	1.1945
3.0000	1.5417	1.5800	0.0383	2.4241
4.0000	0.7768	0.7300	0.0468	6.4066

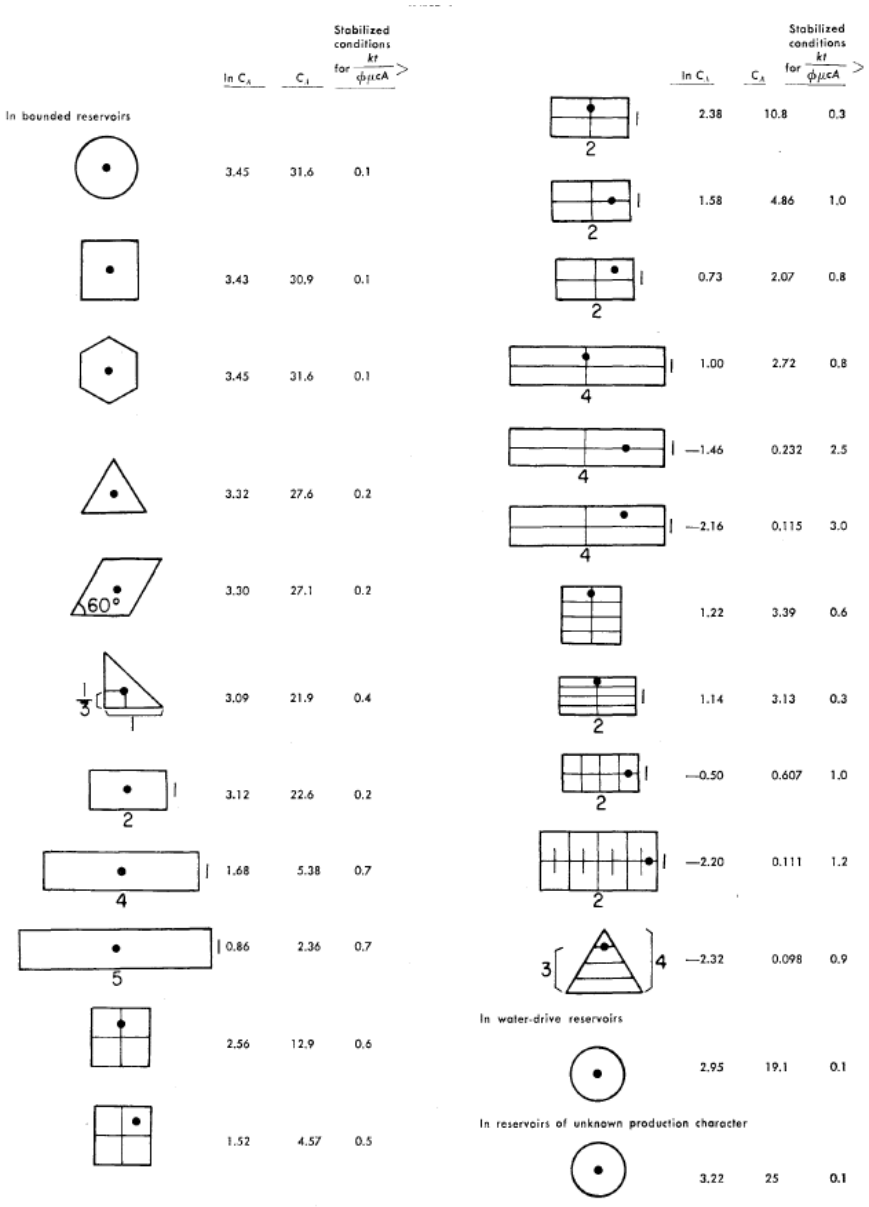

Fig 3.6 Shape factor of several reservoir settings from the Dietz paper

CHAPTER IV

APPLYING THE ASYMPTOTIC SOLUTIONS OF THE DIFFUSIVITY EQUATION TO DETERMINE THE RESERVOIR SHAPE FACTOR

Asymptotic solutions of the diffusivity equation is an alternative approach to the solution of the 3-D diffusivity equation by directly solving the propagation equation for the pressure front defined as the maximum pressure response for an impulse source. This method yields result very close to the known solutions calculated via numerical inversion of the Laplace transform.

$$c_t \frac{\partial p}{\partial t} = \frac{1}{\emptyset A(r)} \frac{\partial q}{\partial r} = \frac{\partial q}{\partial V_p(r)} = -\frac{q_w}{V(t)} e^{-\tau^2/4t} \dots\dots (4.1)$$

$$\frac{d\Delta p_{wf}(t)}{dt} = \frac{q_w(t)}{c_t V(t)} \dots\dots (4.2)$$

In this case we are interested in the fixed rate draw-down in a finite bounded reservoir is a special case of the composite reservoir with no flow boundary.

$$\mathbf{q} = \mathbf{c_t w(\tau)} \frac{\partial \mathbf{p}}{\partial \boldsymbol{\tau}} \dots\dots (4.3)$$

$$\mathbf{w(\tau)} = \frac{\partial \mathbf{V_p}}{\partial \boldsymbol{\tau}} \dots\dots (4.4)$$

We used **Eqn 4.3** and **Eqn 4.4** to Calculate pressure to calculate flow rate as a function of diffusivity time of flight during the pseudo steady state. **Eqn 4.5** and **Eqn 4.6** illustrate the boundary conditions. **Eqn 4.7** related the flow rate at the wellbore to flow rate at a specific diffusivity time of flight. We combined **Eqn 4.3** to **Eqn 4.7** and were able to calculate the relationship between wellbore pressure drop and average reservoir pressure as shown in Eq 4.6.

$$\boldsymbol{\tau} = \mathbf{0}\ \mathbf{q} = \mathbf{q_w}\ \mathbf{V_p} = \mathbf{0} \dots\dots (4.5)$$

$$\tau = \tau_{max}\ q = 0\ V_p = PV \ldots\ldots (4.6)$$

$$q = q_w \frac{PV - V_p(\tau)}{PV} \ldots\ldots (4.7)$$

$$\Delta p_{wf} - \Delta \bar{p} = \frac{q_w}{c_t} \int_{\tau_w}^{\tau_{max}} \frac{d\tau}{w(\tau)} \frac{PV - V_p(\tau)}{PV} \ldots\ldots (4.8)$$

To calculate the average reservoir pressure, we used the definition of the total compressibility as shown in **Eqn 4.9**. After a simple integration, the average pressure drop can be calculated as shown in **Eqn 4.10**.

$$c_t \frac{d\bar{p}}{dt} = \frac{q_w}{PV} \ldots\ldots (4.9)$$

$$\Delta \bar{p} = \frac{q_w t}{c_t (PV)} \ldots\ldots (4.10)$$

The sample calculation is performed to identify the right side of the **Eqn 4.6**. The author used the reservoir properties as shown in **Table 4.1**. **Fig 4.1** shows the evolution of w(τ) for each case. Notice that the graph will approach the reservoir boundary contact area.

Table 4.1 Reservoir properties used in the calculation

property	value	unit
qw	184.44	bbl/day
Δpwf	500	psi
Φ	0.25	
ct	4.2*10^-6	psi^-1
h	107	ft
rw	0.29	ft
re	2900	ft
μ	2.5	cp
k	10.9	mD
Vw	2210	bbl/day
S	707	
xf	250	ft

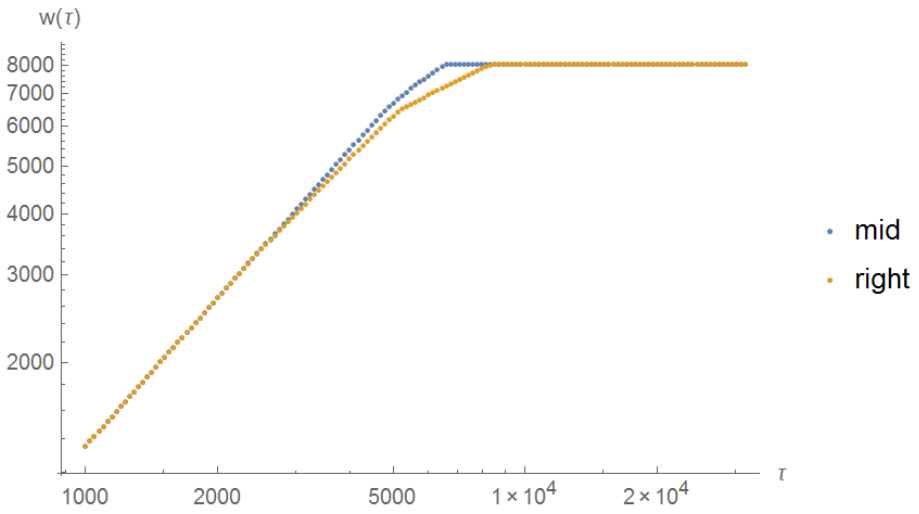

Fig 4.1 Evolution of $w(\tau)$ for each case

Similarly, **Fig 4.2** shows the evolution of Vp (τ) for each case. Notice that the graph will approach the reservoir volume. **Table 4.2 shows** the value of the right hand side of **Eqn 4.8** for each case. However, notice that this value not only depend on the reservoir shape and well location but also on reservoir properties. Therefore, normalization is needed in order to determine the shape factor.

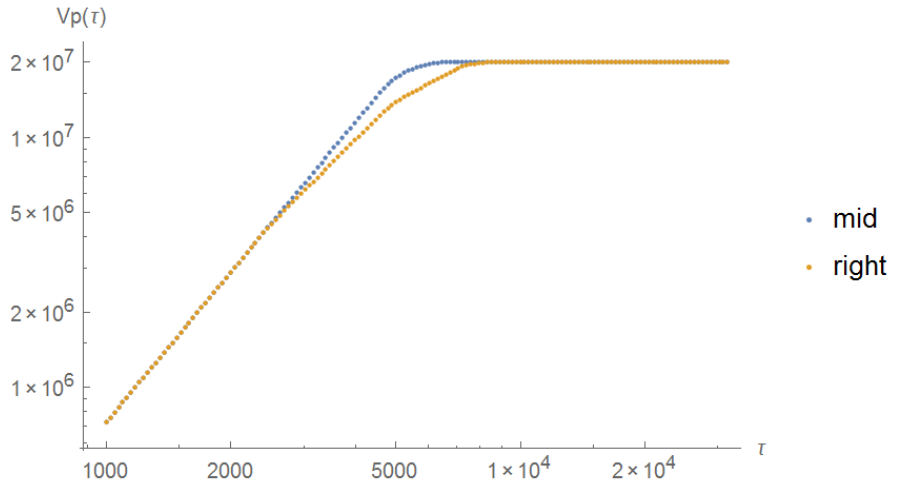

Fig 4.2 Evolution of $V_p(\tau)$ for each case

Table 4.2 the value of the right hand side of Eq 4.6 for each case

cases	difference in pressure drop (psi)
centered well	467.566
off-centered well	473.697

I attempt to write the right side of the **Eqn 4.8** to depend purely on shape factor, which should only depend on the reservoir shape and well location but not reservoir properties. I decompose the τ function to the geometric and reservoir properties part in **Eqn 4.11**. The similar decomposition can be done for $w(\tau)$, V_p, and PV (pore volume) as shown in **Eqn 4.12, Eqn 4.13**, and **Eqn 4.14** respectively.

$$\boldsymbol{\tau = \frac{f(r, rb)}{\sqrt{\frac{k}{\emptyset \mu C_t}}}} \ldots\ldots (4.11)$$

$$\boldsymbol{w(\tau) = f'^{(r,rb)} h \sqrt{\frac{k\emptyset}{\mu C_t}}} \ldots\ldots (4.12)$$

$$\boldsymbol{V_p = f''^{(r^2, rb^2, r*rb)} h\emptyset} \ldots\ldots (4.13)$$

$$\boldsymbol{PV = f'''^{(r^2)} h\emptyset} \ldots\ldots (4.14)$$

$$\boldsymbol{\bar{p} - p_{wf} = \Delta p_{wf} - \Delta \bar{p} = \frac{q_w \mu}{kh} \int_{r_w}^{r_{max}} \frac{d(f(r, rb))}{f'(r, rb)} \frac{f'''(r^2) - f''(r^2, rb^2, r * rb)}{PV}} \ldots\ldots (4.15)$$

After the normalization, I realized the equation can be rearranged in a similar manner as a conventional shape factor equation shown in **Eqn 4.15**, which represents the relationship between average reservoir pressure and bottomhole flowing pressure when the well is produced at a constant flow rate.

$$\Delta p'_{wf} = -\frac{q\mu}{4\pi kh} Ei\left(-\frac{\emptyset \mu c r_w^2}{4k\Delta t}\right) \ldots\ldots (4.16)$$

$$p'_{wf} = p_{wf} + \Delta p'_{wf} \ldots\ldots (4.17)$$

$$\frac{\bar{p} - p'_{wf}}{\frac{q_w \mu}{kh}} = \int_{r_w}^{r_{max}} \frac{d(f(r, rb))}{f'(r, rb)} \frac{f'''(r^2) - f''(r^2, rb^2, r * rb)}{PV} + \frac{1}{4\pi} Ei\left(-\frac{\emptyset \mu c r_w^2}{4k\Delta t}\right) \ldots\ldots (4.18)$$

$$\int_{r_w}^{r_{max}} \frac{d(f(r, rb))}{f'(r, rb)} \frac{f'''(r^2) - f''(r^2, rb^2, r * rb)}{PV} = \text{Geometry Factor} \ldots\ldots (4.19)$$

$$\frac{1}{4\pi} Ei\left(-\frac{\emptyset \mu c r_w^2}{4k\Delta t}\right) + \text{Geometry Factor} = 0 \ldots\ldots (4.20)$$

$$\frac{p^* - p}{\left(\frac{q\mu}{4\pi kh}\right)} = \ln\left(\frac{C_A kt}{\emptyset \mu c A}\right) \ldots\ldots (4.21)$$

$$C_A = \frac{\emptyset \mu c A}{\Delta t_p k} \ldots\ldots (4.22)$$

Table 4.3 the geometric and shape factor of each case

cases	geometry-factor	shape-factor (C_A)
centered well	1.33299	37.4757
off-centered well	1.35047	30.0852

Eqn 4.15 alone is sufficient to determine the geometry factor shown in **Table 4.3.** However, it is important to notice that the geometry factor calculated from the asymptotic solutions of the diffusivity equation (**Eqn 4.19**) has a different definition of the shape factor derived from the one derived from the method of images. However, the geometry factor also serves the same purpose as the old shape factor. They both relate the measured bottom hole pressure to the average reservoir pressure. The geometry factor even has an advantage to the

shape factor because it is much easier to use. Raw bottom hole pressure data plus relevant reservoir properties will suffice. On the other hand, the old method using shape factor needs an engineers to plot the graph between bottom hole pressure and the Honor time ratio.

To transform the geometry factor to shape factor, we need to calculate the bottomhole flowing pressure after the well has been shut in. **Eqn 4.19** shows the bottomhole pressure increase after shut in. To determine the shape factor, the time causing bottomhole flowing pressure is equal to average reservoir pressure will be determined as shown in **Eqn 4.20**. Based on **Eqn 4.21**, shape factor can be found by **Eqn 4.22**. Δt_p is the time on Honor plot that bottomhole flowing pressure is equal to average reservoir pressure. Table 4.3 shows the shape factor of each case. The calculated shape factors agree fairly well with the ones from image well for the centered well case. Currently, the author is working on the off-centered well to investigate how to make both shape factors agree better.

CHAPTER V

CONCLUSION

To conclude, in this work we have successfully extended the concept of drainage volume to be applied to fractures. By using analytical methods to incorporate interference effects, we are able to derive an approach to summarize well drainage volume taking into account the performance of each fracture. By comparing our calculated well drainage volume to a set of theoretical bounds, we determined that our methodology is reasonable.

We successfully calculate the new “shape factor” (geometry factor) from the asymptotic solutions of the diffusivity equation. The new “shape factor” only requires raw bottom hole pressure data plus relevant reservoir properties in order to calculate the average reservoir pressure. On the other hand, the old method needs an engineers to plot the graph between bottom hole pressure and the Horner time ratio.

WORKS CITED

Dietz, D. N. (1965). Determination of Average Reservoir Pressure From Build-Up Surveys. Journal of Petroleum Technology: 955-959. *Society of Petroleum Engineers.* doi:10.2118/1156-PA

King, M.J., Wang, Z. and Datta-Gupta, A. (2016). Asymptotic Solutions of the Diffusivity Equation and Their Applications. SPE Europec/EAGE Annual Conference and Exhibition, Vienna, Austria, May 30 – June 2. SPE-180149-MS. DOI: 10.2118/180149-MS.

Lee, J., Rollins, J.B. and Spivey, J.P. (2003). Pressure Transient Testing. *Society of Petroleum Engineers.*

Matthews, C. S., Brons, F., & Hazebroek, P. (1954) A Method for Determination of Average Pressure in a Bounded Reservoir. Petroleum Transactions. AIME: 182-191 Society of Petroleum Engineers.

Song, B., Economides, M. J., & Ehlig-Economides, C. (2011). Design of Multiple Transverse Fracture Horizontal Wells in Shale Gas Reservoirs. SPE Hydraulic Fracturing Technology Conference and Exhibition, Woodlands, TX, USA, Jan 24 – 26. SPE-1405550-MS. DOI: 10.2118/140555-MS.

Winestock, A.G., and Colpitts, G.P. (1965). Advances in Estimating Gas Well Deliverability, *Petroleum Society of Canada.*

Yang, C., Sharma, V.K., Datta-Gupta, A. and King, M.J. (2015). A Novel Approach for Production Transient Analysis of Shale Gas/Oil Reservoirs. Unconventional Resources Technology Conference, San Antonio, Texas, July 20-22, 2015. SPE-178714-MS.